MOF-aided topotactic transformation into nitrogen-doped porous Mo$_2$C mesocrystals for upgrading pH-universal hydrogen evolution reaction

Tengteng Gu,[a,b] Rongjian Sa,[c] Linjie Zhang,[b] Feng Zhou,[b] Ruihu Wang[b] and Xiaoju Li[a]*

[a]Fujian Key Laboratory of Polymer Materials, College of Chemistry and Materials Science, Fujian Normal University, Fuzhou, Fujian 350007, China

[b]State Key Laboratory of Structural Chemistry, Fujian Institute of Research on the Structure of Matter, Chinese Academy of Sciences, Fuzhou, Fujian 350002, China

[c]Institute of Oceanography, Ocean College, Minjiang University, Fuzhou, Fujian 350108, China

Experimental section

Materials. All chemicals were commercially available and used without further purification. Molybdenum powder, cobalt nitrate hexahydrate, 2-methylimidazole, polyvinyl pyrrolidone (PVP) and nafion solution (5 wt%) were purchased from Sigma Aldrich. Hydrogen peroxide, methanol, sulfuric acid and potassium hydroxide were purchased from Sinopharm Chemical Reagent. Potassium hydrogen phosphate anhydrous and potassium phosphate monobasic were purchased from Aladdin Reagent. Pt/C (20 wt%) was purchased from Alfa Aesar. Ultrapure water (18.25 MΩ cm^{-1}) was produced by a Water Purifier system.

Pretreatment of CFP. CFP was electrochemically activated according to the modified literature method.[S1] Briefly, a CFP slip (2×3 cm^2) was immersed in 0.5 M aqueous H_2SO_4 solution and used as the working electrode in a conventional three-electrode cell at room temperature. Ag/AgCl and graphite rod were used as the reference and counter electrodes, respectively. After CFP was activated by cyclic voltammetry between 1.5 and 2.0 V versus SCE with a scan rate of 10 mV s^{-1} for 50 cycles,[S2,S3] the resultant CFP was rinsed in ultrapure water several times to remove the residual acidic electrolyte, and then dried in air to afford the pretreated CFP.

Synthesis of MoO₃·H₂O/CFP. 1.0 g of molybdenum powder was slowly added into 4 mL of H_2O_2 solution under stirring. After it was completely dissolved, 96 mL of ultrapure water was added and the mixture was stirred until the color of the solution turns into dark blue. After the solution was purged with nitrogen for 15 min and was directly used as the electrolyte. The pretreated CFP slip was vertically immersed in the above electrolyte as the working electrode. Saturated Ag/AgCl electrode and graphite rod were used as the reference and counter

electrodes, respectively. $MoO_3 \cdot H_2O/CFP-x$ was obtained by electrodeposition at -0.6 V vs sat. Ag/AgCl for appropriate time, where x refers to the electrodeposition time.

Synthesis of MoO₃/CFP-*x*. The as-synthesized ZIF-67 nanocrystals (90 mg) were finely ground into powders and were loaded at the bottom of a quartz socket tube, $MoO_3/CFP-x$ (1×2 cm^2) was leaned on the other end of the quartz socket tube, and the quartz bushing was located at the center heating zone of tubular furnace. The samples were heated to 800 °C under 10% H_2/Ar atmosphere with a heating rate of 5 °C min^{-1} and kept at 800 °C for 2 h. N-$Mo_2C/CFP-x$ was attained after naturally cooling to ambient temperature.

Characterizations

Scanning electron microscope (SEM) and transmission electron microscopy (TEM) images were acquired on Hitachi SU8010 and FEI Tecnai F30 instruments, respectively. Powder X-ray diffraction (XRD) was recorded on a Mini Flex 600 diffractometer. Nitrogen adsorption/desorption data were recorded at liquid nitrogen temperature (77 K) using a Micromeritics ASAP 2020 M apparatus. The sample was degassed at 120 °C under vacuum for 12 h prior to the measurement. The specific surface area was calculated using the Brunauer-Emmett-Teller (BET) equation, and the total pore volumes were calculated from the amount adsorbed at a relative pressure (P/P$_0$) of 0.99. The pore size distributions were calculated by the nonlocal density functional theory (NL-DFT) model. The Raman measurements were performed on a Renishaw spectrometer at 532 nm on a Renishaw Microscope System RM2000. X-ray photoelectron spectroscopy (XPS) was conducted on a Thermo Scientific ESCALAB spectrometer. Elemental analysis was operated on a Vario MICRO elemental analyzer. Inductive coupling plasma-optical emission spectroscopy (ICP-

OES) was performed on a Jobin Yvon Ultima 2 system. X-ray absorption fine structure (EXAFS) measurements were conducted to investigate the local structures of the Mo composite catalysts at the beamline 14W1 in 1W1B station in Beijing Synchrotron Radiation Facility (BSRF). The incident beam was monochromatized using a Si (111) double crystal monochromator. At room temperature, the spectra were taken for the K-edge of Mo (E0 = $2.0*10^4$ eV) in a transmission mode with separate N_2-filled IC Spec ionization chambers for incident and transmitted beams. The reference spectra of Mo foil were taken simultaneously so that the energy in the spectrum of sample could be calibrated with the respect to the K-edge energy of Mo metal. The obtained data were analyzed with ATHENA and ARTEMIS in the IFEFIT suite of software programs. FEFF9 code was used to synthesize theoretical EXAFS spectra for nonlinear square fitting of samples.

Electrochemical measurements

All samples were tested on a CHI 760E electrochemical workstation with a three-electrode system. The self-supported $N-Mo_2C/CFP$ was directly served as a working electrode, and graphite rod was used as a counter electrode. For reference electrode used in electrolytes with different pH value, a saturated calomel electrode (SCE) was chosen for aqueous 0.5 M H_2SO_4, while a saturated Ag/AgCl electrode was used for both aqueous 1 M KOH and 1 M PBS solutions. Unless otherwise stated, all potentials were reported versus reversible hydrogen electrode (RHE) by converting the potentials measured according to the following equation: E (*vs*. RHE) = E (*vs*. Ref.) + E°$_{ref.}$ (*vs*. SHE) + 0.059 × pH, and all potentials in this study were *iR*-compensated. To evaluate the electrocatalytic HER activity, cathodic linear sweep voltammetry (LSV) curves were measured at a scan rate of 5 mV s^{-1} in static Ar-saturated

electrolytes under constant room temperature of 25 °C. Cyclic voltammetry (CV) under non-Faradaic potentials was used to detect electrochemical double-layer capacitance for estimating the effective electrochemical active area. Electrochemical impedance spectroscopy (EIS) spectra were performed with frequency from 10^{-2} to 10^{6} Hz with an amplitude of 10 mV. The long-term durability of the catalysts was tested by the chronoamperometry for 24 h, and the continuously repeated 1000 CV cycles as well.

Calculation of ECSA

The electrochemical double-layer capacitances (C_{dl}) of the electrocatalysts are obtained based on the equation:

$C_{dl} = I / K$

Where K is the scan rate.

ECSA is calculated by assuming a standard value of 60 μF cm^{-2} [S4]:

$ECSA = C_{dl} / 60$

Turnover Frequency (TOF) Calculation.

Turnover frequency (TOF) values of different samples were calculated according to the equation:

$TOF = J * N_A / (2 * n * F * ECSA)$

Where J is the current density, N_A is the Avogadr's number, 2 represents the stoichiometric number of electrons consumed in the electrode HER reaction, n is the number of the active sites, F is the Faraday constant and ECSA is the electrochemically active surface area of the electrode.

Computational Details

Density functional theory (DFT) calculations have been applied to investigate hydrogen evolution reaction (HER) process of Mo_2C and $N-Mo_2C$ systems. The initial structure of Mo_2C was taken from bulk Mo_2C with A $2 \times 2 \times 1$ supercell. The optimized cell parameters are $a = 6.063$ Å, $b = 6.071$ Å and $c = 4.726$ Å.[S5] The Mo_2C (002) slab was used to evaluate the HER process. Along the [002] direction, Mo_2C showed two different crystal planes with Mo atoms on the top plane and C atoms on the bottom plane (Mo_2C-MoT and $N-Mo_2C-MoT$) or with C atoms on the top plane and Mo atoms on the bottom plane (Mo_2C-CT and $N-Mo_2C-CT$). All calculations were carried out by using DMo_{l3} package.[S6] The generalized gradient approximation (GGA) with the functional of Perdew-Burke-Ernzerhof (PBE) was utilized. DFT semi-core pseudopotentials were used for the core treatment with a double numerical polarized (DNP) 3.5 basis set. The Grimme's scheme was adopted to treat the long-range dispersion interactions. A Fermi smearing of 0.005 hartree was utilized in this calculation. The convergence criteria for energy, gradient and displacement convergence were 1.0×10^{-5} Ha, 0.002 Ha/Å, and 0.005 Å, respectively. $5 \times 5 \times 5$ and $3 \times 3 \times 2$ Monkhorst-Pack grid for the Brillouin zone sampling were used for bulk and slab Mo_2C models, respectively. The Mo_2C (002) slab model was six thick layers and a (2×2) surface unit cell with 48 Mo atoms and 24 C atoms. All periodic slabs had a vacuum spacing of at least 15 Å, which was thick enough to avoid artificial interaction. All atoms in the bottom layers were fixed to the bulk positions, while the adsorbate and the atoms in the top two layers were allowed to relax. The free energy of HER process was evaluated by following equation: $\Delta G = \Delta E - E_H + \Delta E_{ZPE} - T\Delta S$. ΔE is the difference between the energy of the adsorption state and pure surface, E_H is the energy of H in gas phase, E_{ZPE} is the zero-point energy change and ΔS is the entropy change.
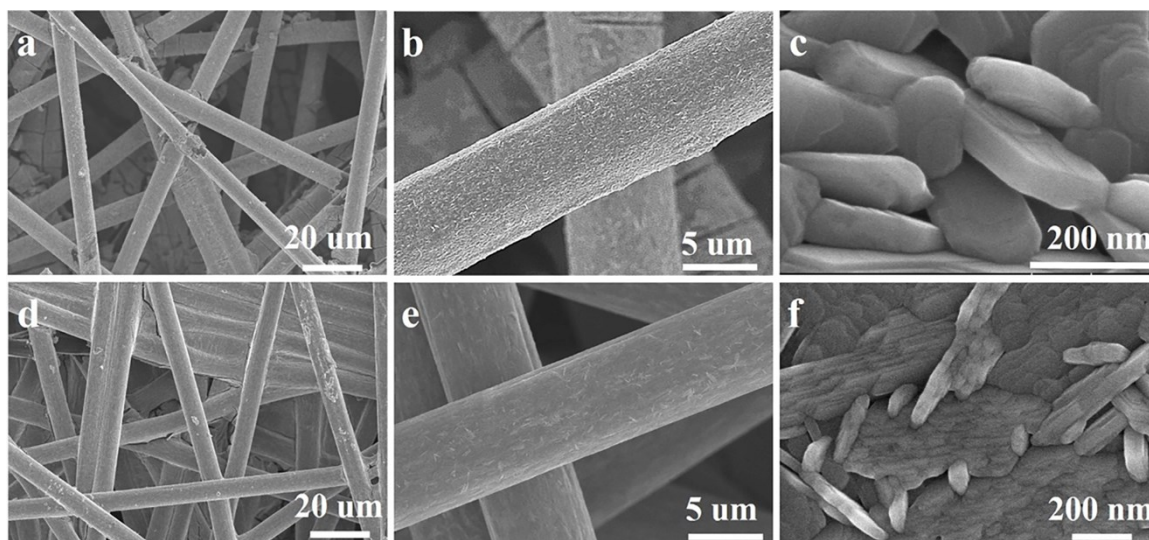
Fig. S1. The digital photograph for the quartz socket tube loaded with ZIF-67 and MoO$_3$/CFP inside two sides.
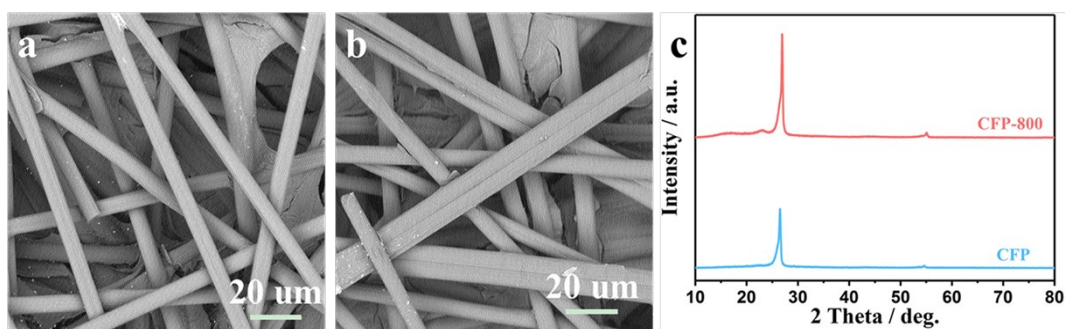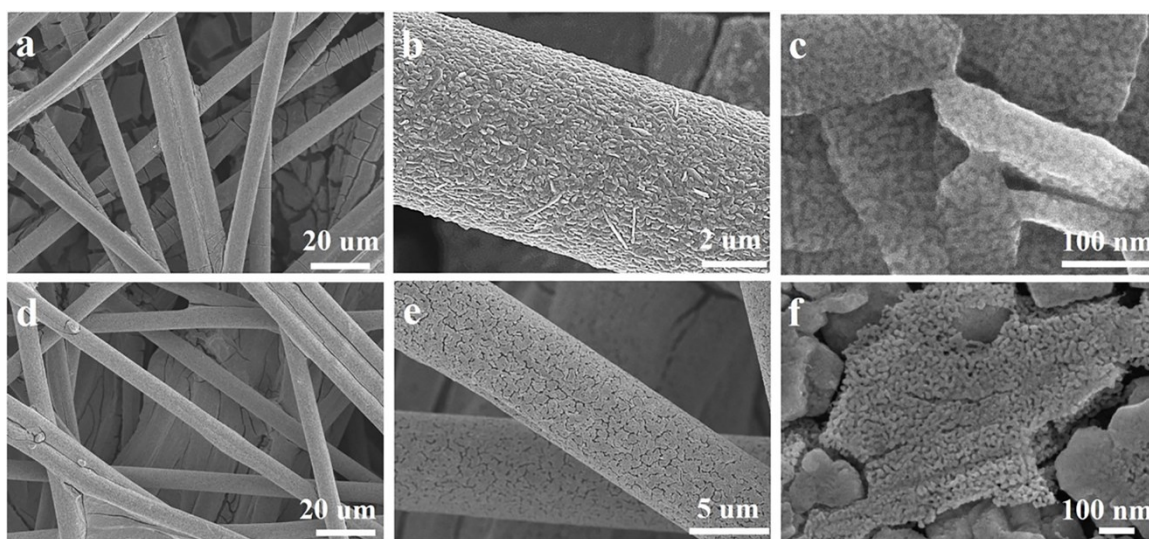

Fig. S2. SEM images of (a) pristine CFP and (b) CFP after calcination at 800 $^\circ$C (CFP-800) under 10% H$_2$/Ar atmosphere. c) XRD patterns for CFP and CFP-800.
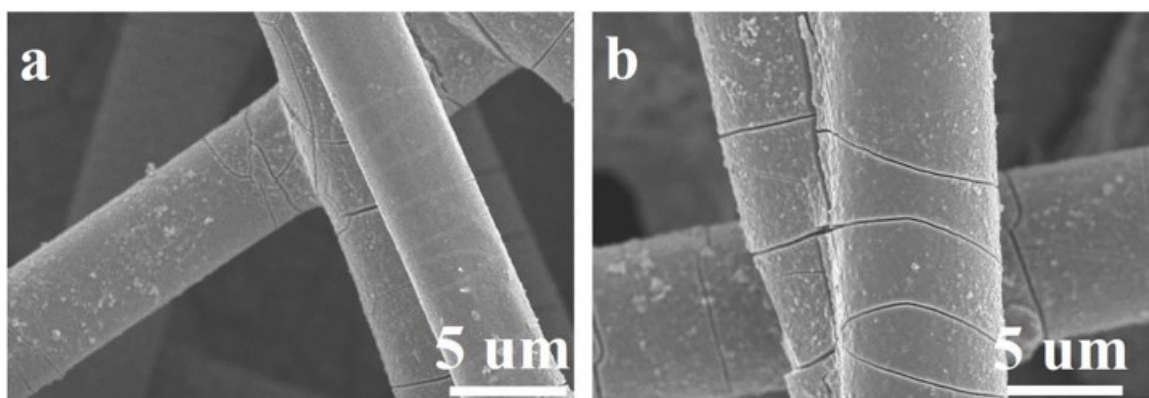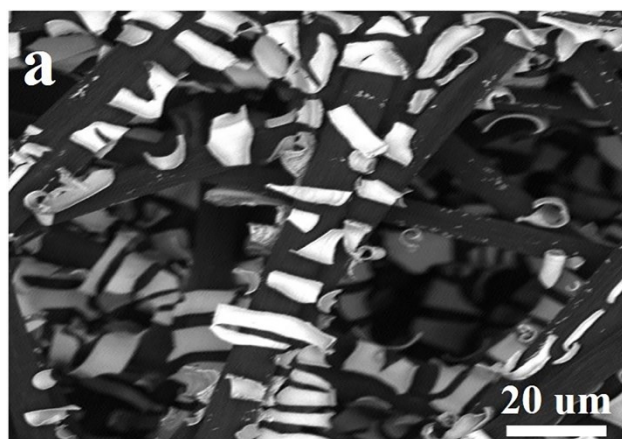
Fig. S3. SEM images for (a) $MoO_3 \cdot H_2O$/CFP-30 and (b) $MoO_3 \cdot H_2O$/CFP-60.

Fig. S4. SEM images for (a-c) MoO_3/CFP-30 and (d-f) MoO_3/CFP-60.

Fig. S5. SEM images for (a-c) N-Mo$_2$C/CFP-30 and (d-f) N-Mo$_2$C/CFP-60.

Fig. S6. SEM image for the sample obtained through direct carbonization of MoO$_3$·H$_2$O/CFP-45.
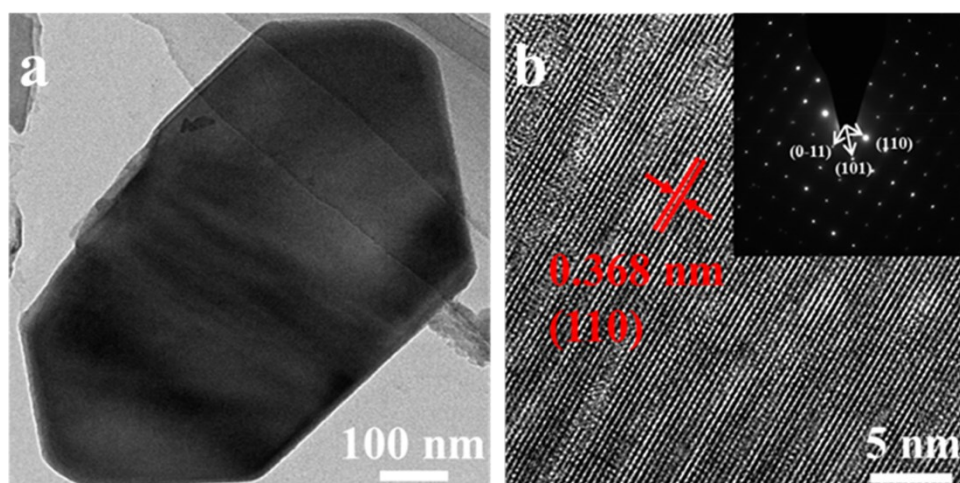
Fig. S7. (a) TEM and (b) HRTEM images for MoO_3/CFP-45, the inset in b is the electron-diffraction pattern.
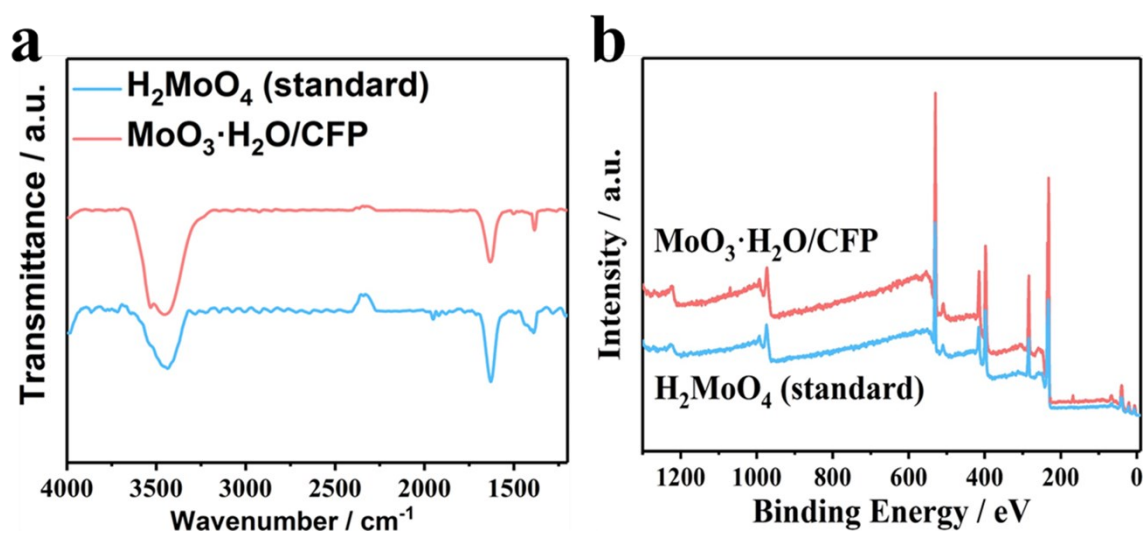
Figure S8. (a) FTIR and (b) XPS survey spectra for $MoO_3 \cdot H_2O$/CFP and standard molybdic acid.
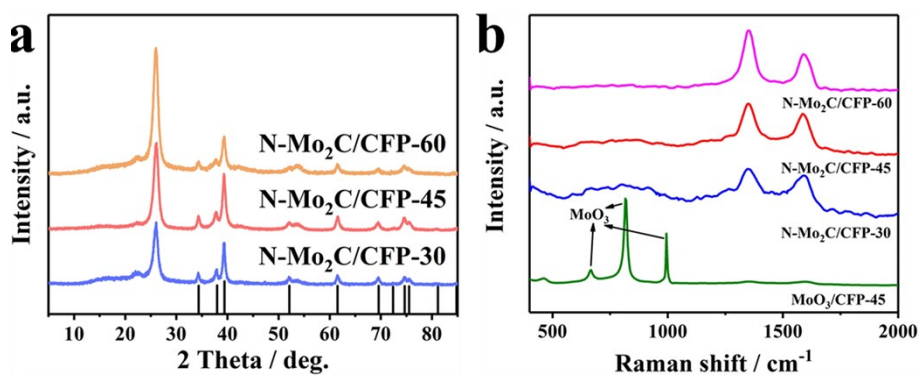
Fig. S9. (a) XRD patterns and Raman spectra for N-Mo$_2$C/CFP-30, N-Mo$_2$C/CFP-45 and N-Mo$_2$C/CFP-60.
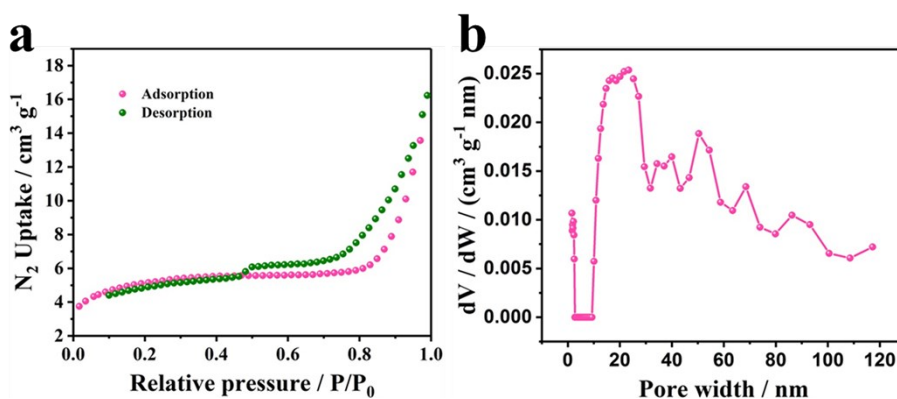

Fig. S10. (a) N$_2$ adsorption isotherm and (b) corresponding pore size distribution for N-Mo$_2$C scratched from N-Mo$_2$C/CFP-45.
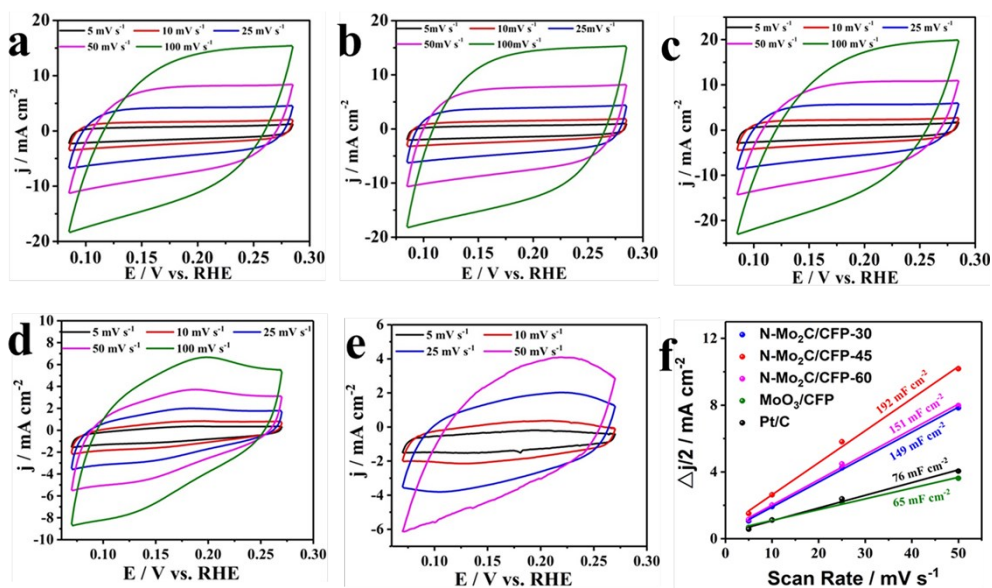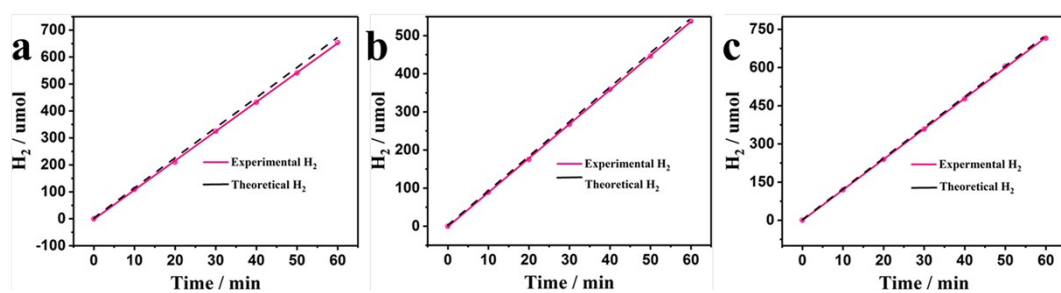
Fig. S11. Electrochemical capacitance measurements for (a) N-Mo$_2$C/CFP-30, (b) N-Mo$_2$C/CFP-45, (c) N-Mo$_2$C/CFP-60, (d) MoO$_3$/CFP-45 and (e) 20wt% Pt/C in 0.5 M H$_2$SO$_4$ using CV at various scan rates. (f) Difference in current density plotted against scan rate showing the extraction of C$_{dl}$ value.
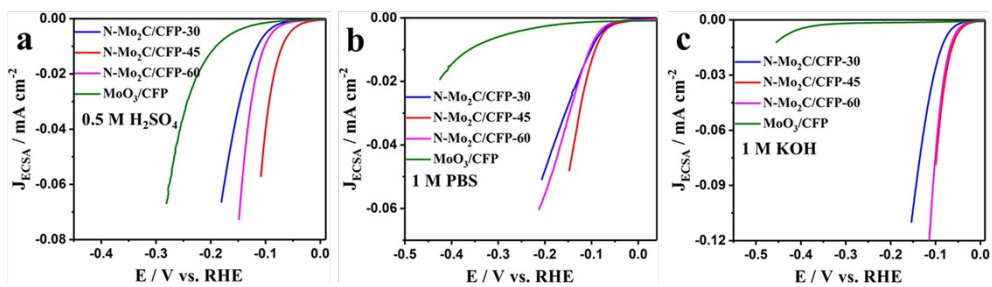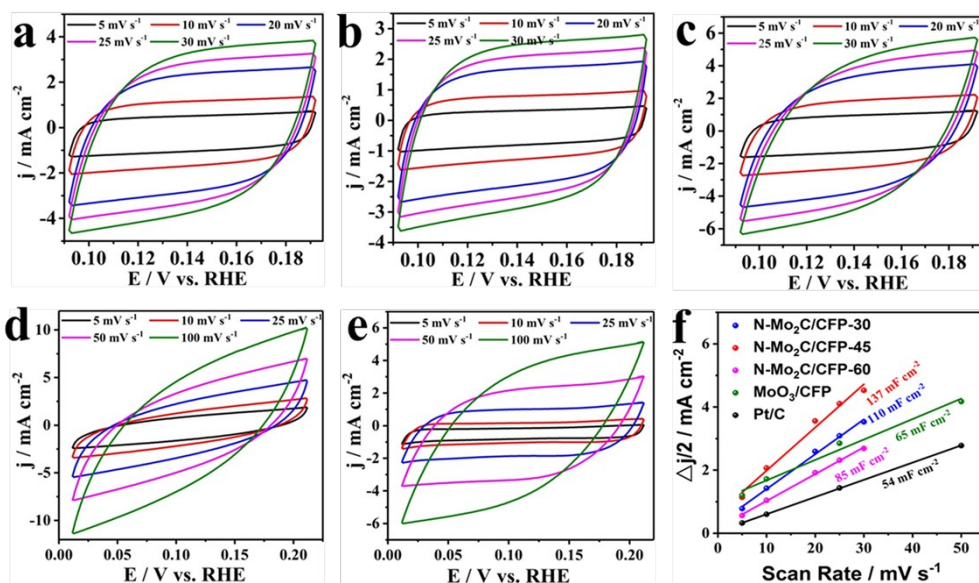

Fig. S12. ECSA-normalized HER polarization curves for N-Mo$_2$C/CFP-x and MoO$_3$/CFP-45 in (a) 0.5 M H$_2$SO$_4$, (b) 1.0 M PBS and (c) 1.0 M KOH.

S 12
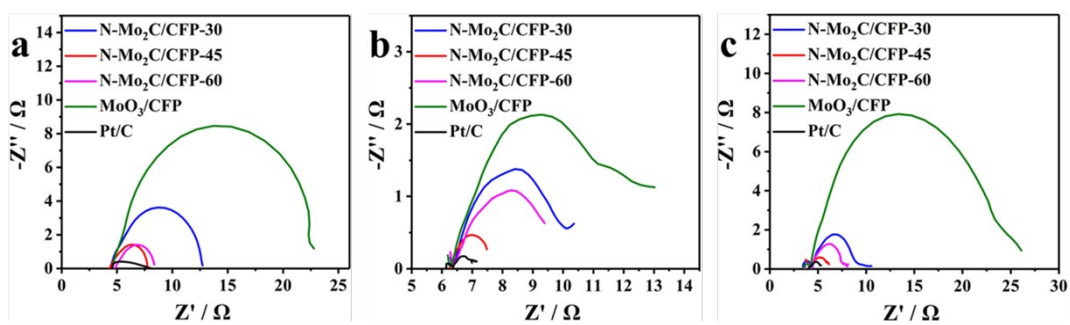
Fig. S13. EIS spectra in (a) 0.5 M H_2SO_4, (b) 1 M PBS and (c) 1 M KOH for N-Mo_2C/CFP-*x*, MoO_3/CFP-45 and Pt/C.


<mark>**Fig. S14.** The amount of hydrogen production at different reaction time for N-Mo_2C/CFP-45 in (a) 0.5 M H_2SO_4, (b) 1.0 M PBS and (c) 1.0 M KOH.</mark>

Fig. S15. Electrochemical capacitance measurements for (a) N-Mo$_2$C/CFP-30, (b) N-Mo$_2$C/CFP-45, (c) N-Mo$_2$C/CFP-60, (d) MoO$_3$/CFP-45 and (e) 20 wt% Pt/C in 1 M PBS using CV at various scan rates. (f) Difference in current density plotted against scan rate showing the extraction of C$_{dl}$ value.
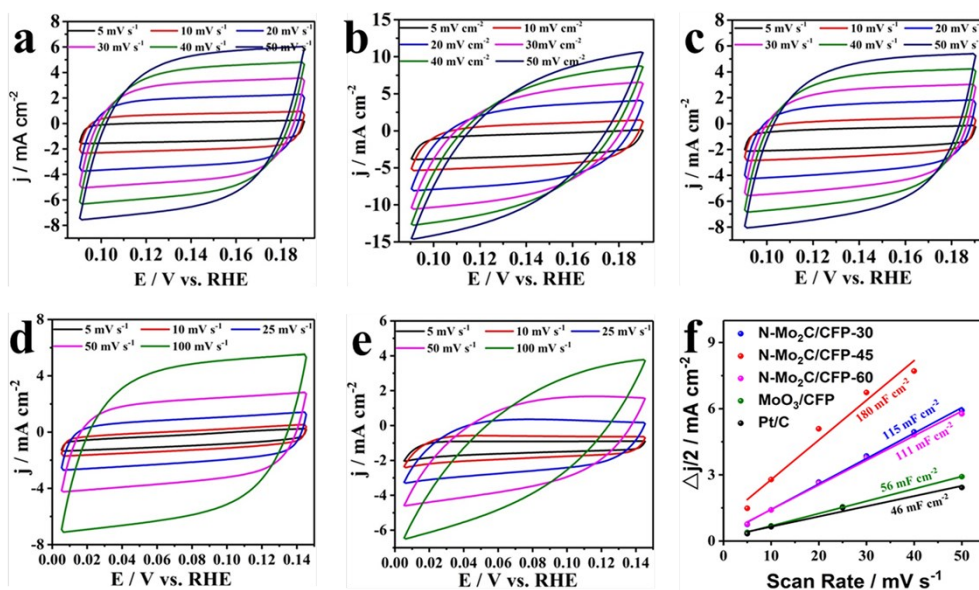
Fig. S16. Electrochemical capacitance measurements for (a) N-Mo$_2$C/CFP-30, (b) N-Mo$_2$C/CFP-45, (c) N-Mo$_2$C/CFP-60, (d) MoO$_3$/CFP-45 and (e) 20 wt% Pt/C in 1 M KOH using CV at various scan rates. (f) Difference in current density plotted against scan rate showing the extraction of C$_{dl}$ value.
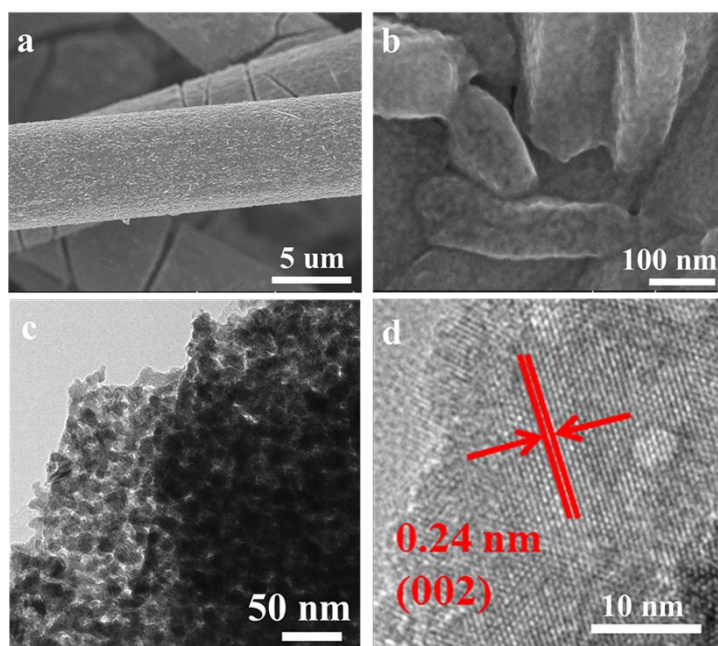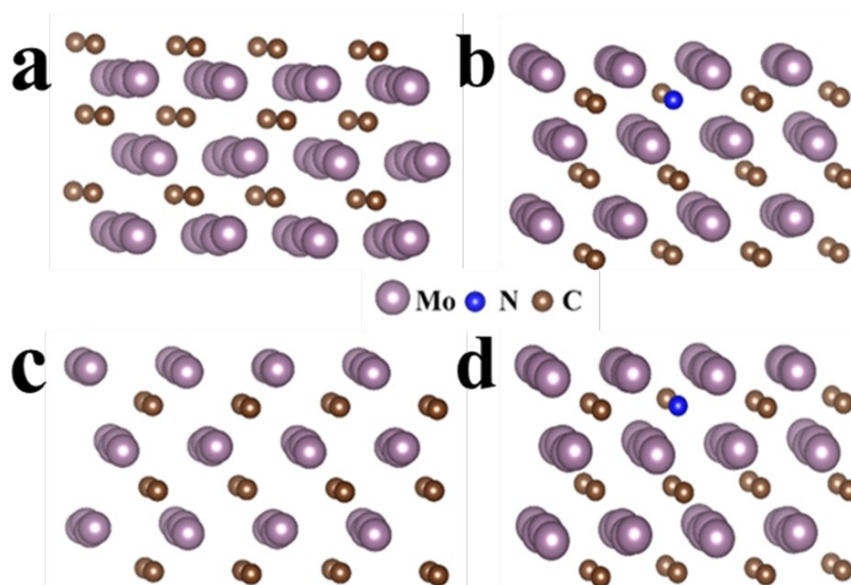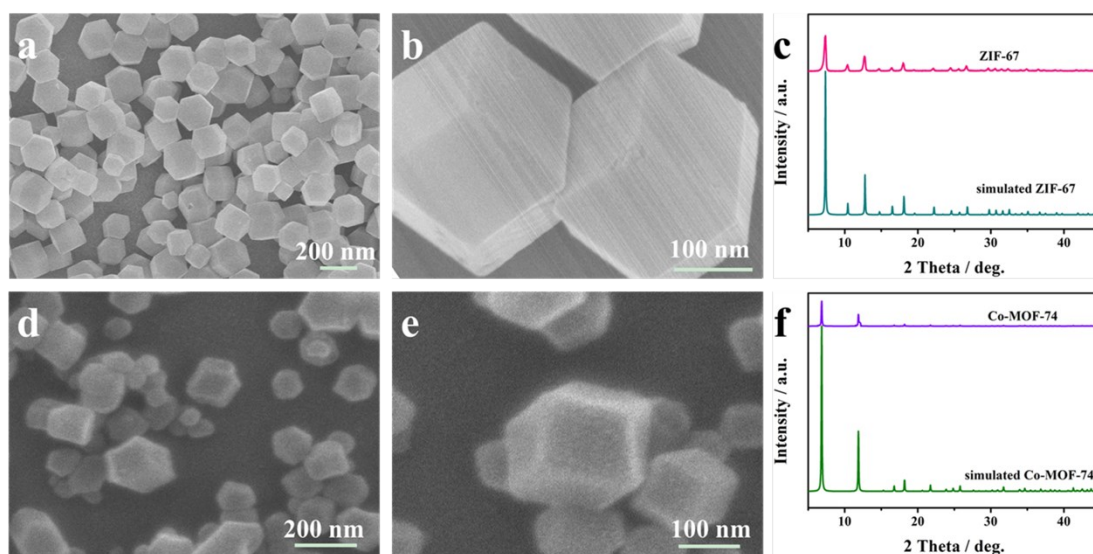
Fig. S17. (a, b) SEM, (c)TEM and (d) HRTEM images of N-Mo$_2$C/CFP-45 after HER durability test in 1 M KOH.
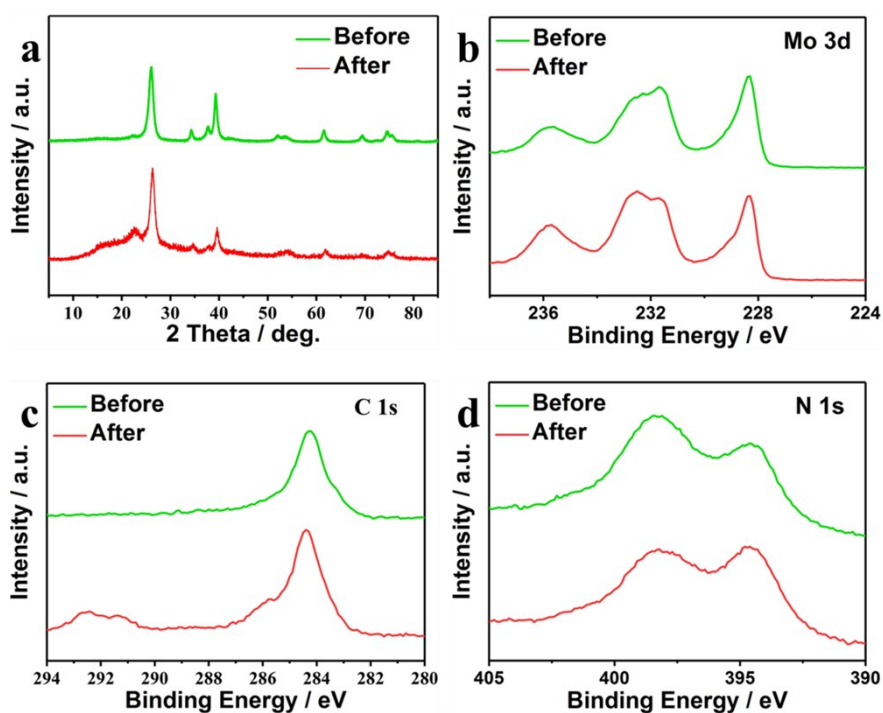
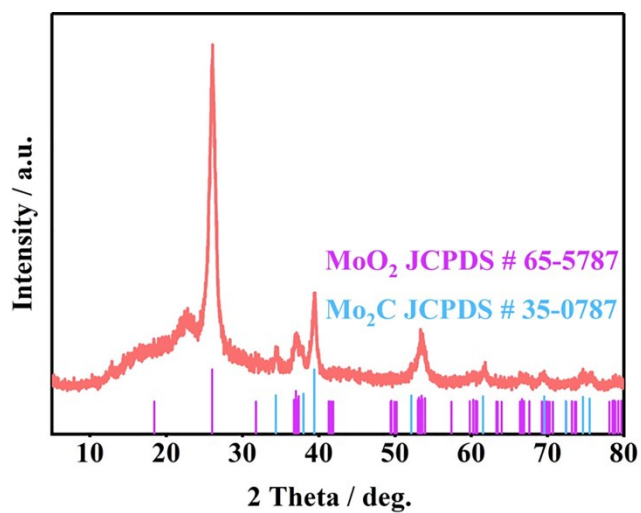**Fig. S18.** (a) XRD pattern, (b) Mo 3d, (c) C 1s and (d) N 1s XPS spectra of N-Mo$_2$C/CFP-45 before and after HER durability test in 1 M KOH.

Fig. S19. Side view of the optimized geometries on (002) facet for (a) Mo_2C-CT (b) N-Mo_2C-CT (c) Mo_2C-MoT and (d) N-Mo_2C-MoT.

Fig. S20. (a, b) SEM images and (c) XRD patterns for ZIF-67. (d, e) SEM images and (f) XRD pattern for Co-MOF-74.

Fig. S21. XRD pattern of Mo_2C-MoO_2/CFP obtained using Co-MOF-74 as carbon source.
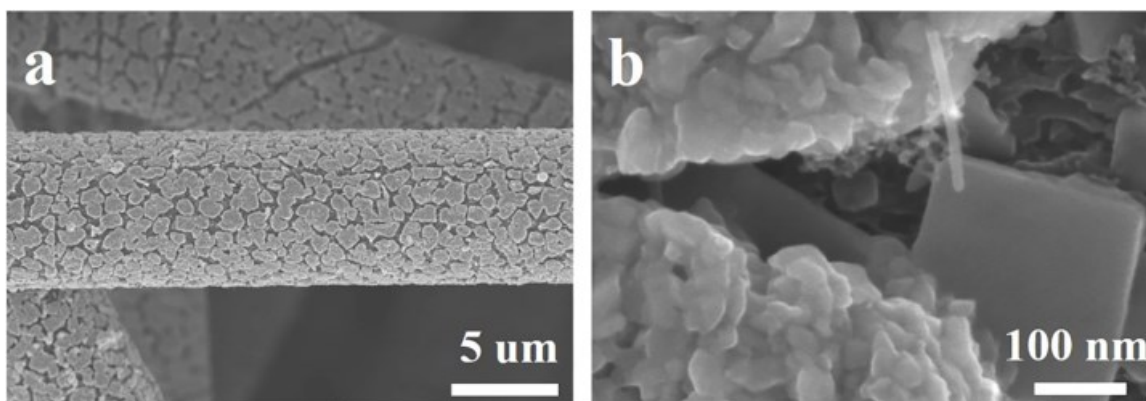
Fig. S22. (a, b) SEM images of Mo_2C/MoO_2-CFP obtained using Co-MOF-74 as carbon source.
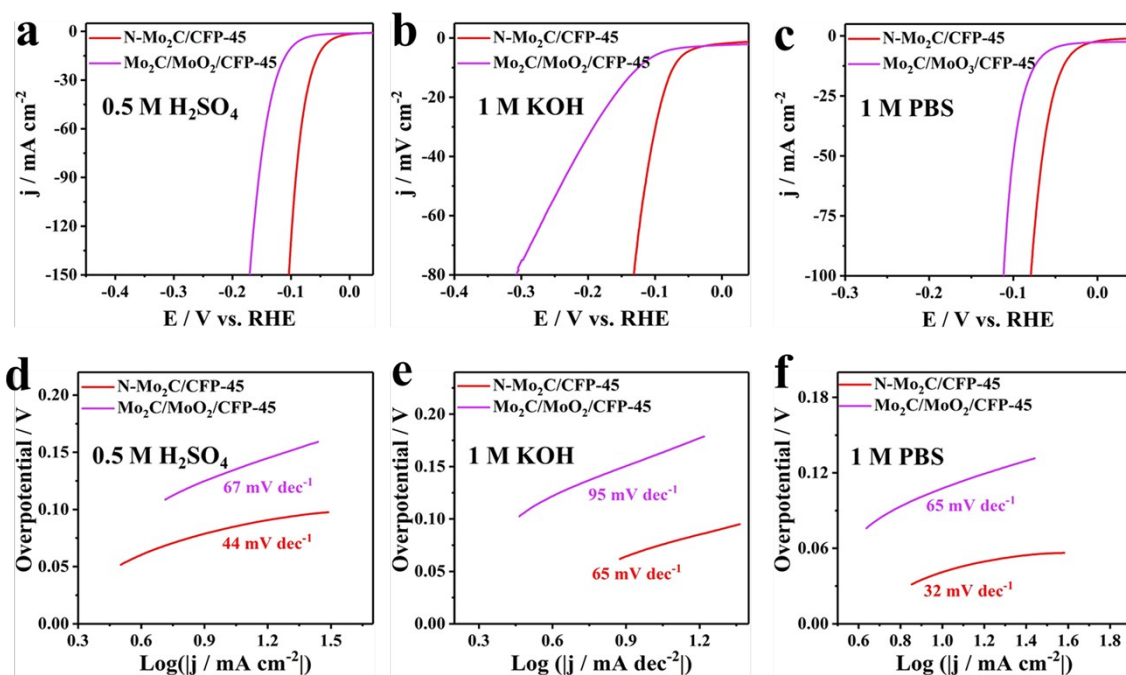
Fig. S23. (a, b, c) HER polarization curves and (d, e, f) Tafel plots for N-Mo$_2$C/CFP-45 and Mo$_2$C/MoO$_2$/CFP-45 in 0.5 M H$_2$SO$_4$, 1 M PBS and 1 M KOH electrolytes.
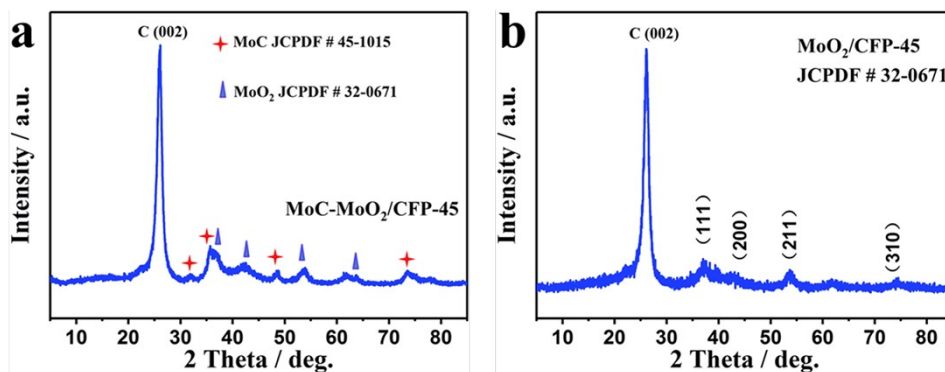
Fig. S24. XRD patterns for (a) MoC-MoO$_2$/CFP-45 obtained using ZIF-8 as carbon and nitrogen sources and (b) MoO$_2$/CFP-45 obtained using 2-methylimidazole as carbon and nitrogen sources.
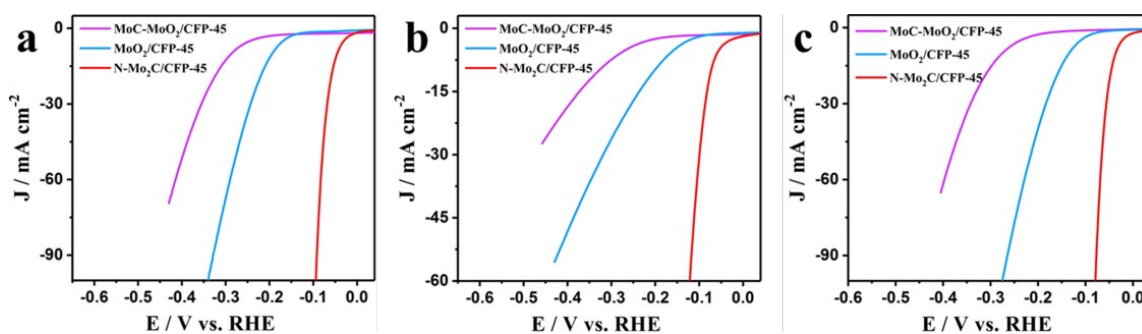
Fig. S25. HER polarization curves for MoC-MoO$_2$/CFP-45, MoO$_2$/CFP-45 and N-Mo$_2$C/CFP-45 in (a) 0.5 M H$_2$SO$_4$, (b) 1 M PBS and (c) 1 M KOH.
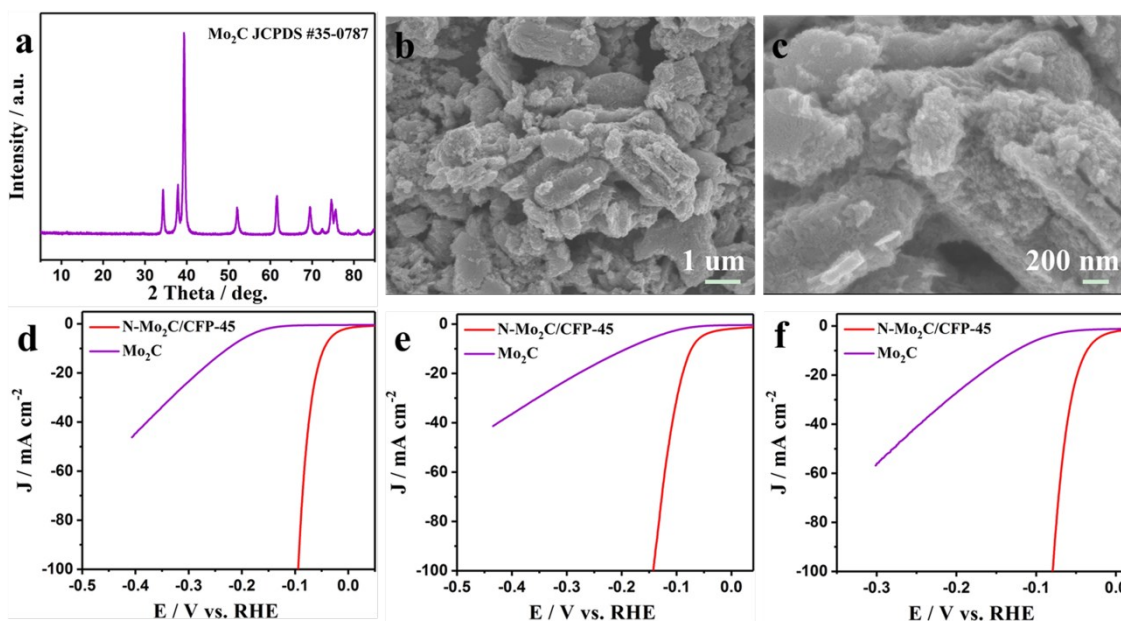
Fig. S26. (a) XRD pattern and (b, c) SEM images for Mo$_2$C synthesized without CFP; Polarization curves of N-Mo$_2$C/CFP-45 and Mo$_2$C electrodes in (d) 0.5 M H$_2$SO$_4$, (e) 1 M PBS and (f) 1 M KOH.
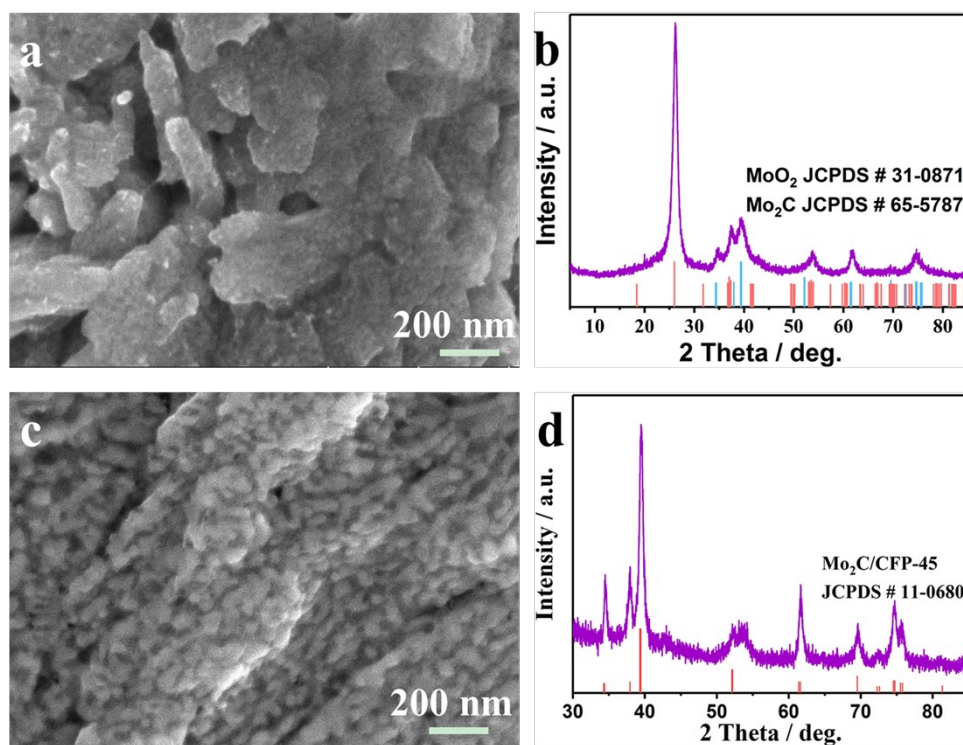
Fig. S27. (a) SEM image and (b) XRD pattern of MoO_2-Mo_2C/CFP obtained at 700 °C. (c) SEM image and (d) XRD pattern of Mo_2C/CFP obtained at 900 °C.
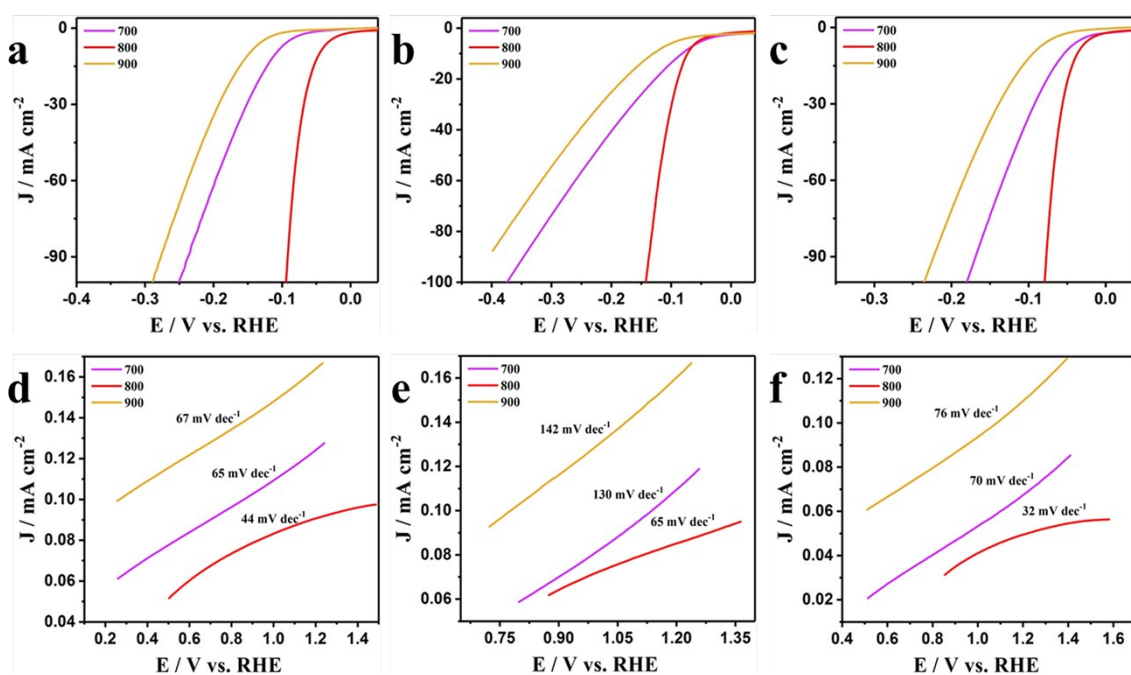
Fig. S28. HER polarization curves and Tafel plots for N-Mo_2C/CFP-45 obtained at different calcination temperatures in (a, d) 0.5 M H_2SO_4, (b, e) 1.0 M PBS and (c, f) 1.0 M KOH.

Table S1. The mass loading densities of Mo species in $MoO_3 \cdot H_2O$/CFP-*x*, MoO_3/CFP-*x* and N-Mo_2C/CFP-*x*.

x/min	The mass loading of Mo species (mg cm^{-2})		
	$MoO_3 \cdot H_2O$/CFP-x	MoO_3/CFP-x	N-Mo_2C/CFP-x
30	5.35	2.32	2.70
45	7.78	3.17	3.45
60	9.55	4.70	4.10

Table S2. Elemental contents of N-Mo_2C/CFP-*x*.

Samples	Mo/wt% [a]	C/wt% [b]	N/wt% [b]
N-Mo_2C/CFP-30	20.74	70.24	5.87
N-Mo_2C/CFP-45	23.83	65.72	7.64
N-Mo_2C/CFP-60	28.93	63.29	6.78

[a] Measured by ICP-OES; [b] Measured by elemental analysis.

Table S3. Comparison of HER performance for N-Mo_2C/CFP-45 with the reported noble-metal-free electrocatalysts in 0.5 M H_2SO_4. η_{10} is denoted as overpotential at -10 mA cm^{-2}.

Catalyst	η_{onset} (mV)	η_{10} (mV)	Tafel slope (mV dec^{-1})	Reference
N-Mo_2C/CFP-45	11	45	44	This work
Co-NRCNTs	140	260	69	[S7]
FeP Nanoparticles	--	50	37	[S8]
Mo_xC-IOL	79	117	60	[S9]
Mo_5N_6 NSs	--	~249	330	[S10]
Ni_2P@NPCNFs	52	63.2	56.7	[S11]
MoP_2 NSs	--	58	98	[S12]
MoP NS/CC	50	187	94	[S13]
Mo_2C nanowires	70	200	53	[S14]
Co-Mo_2C	40	140	39	[S15]
MoCN	50	140	46	[S16]
$FePSe_3$/NC	--	70	53	[S17]
(CNF)@CoS_2	40	110	66.8	[S18]
$Cu_{0.075}Co_{0.925}P$/CP	--	47	47.2	[S19]
Mo_2C	14	35	25	[S20]

Table S4. C_{dl} and ECSA of MoO_3/CFP, N-Mo_2C/CFP-30, N-Mo_2C/CFP-45 and N-Mo_2C/CFP-60 in 0.5 M H_2SO_4, 1.0 M PBS and 1.0 M KOH.

Catalysts	0.5 M H_2SO_4		1 M PBS		1 M KOH	
	C_{dl} (mF cm^{-2})	ECSA (cm^2)	C_{dl} (mF cm^{-2})	ECSA (cm^2)	C_{dl} (mF cm^{-2})	ECSA (cm^2)
MoO_3/CFP	65	541	65	541	56	466
N-Mo_2C/CFP-30	149	1241	110	916	115	958
N-Mo_2C/CFP-45	192	1600	137	1141	180	1500
N-Mo_2C/CFP-60	151	1258	85	708	111	925

Table S5. Comparison of HER performances for N-Mo$_2$C/CFP-45 with other non-noble metal-based electrocatalysts in 1 M PBS. η_{10} is denoted as overpotential at -10 mA cm^{-2}.

Catalyst	η_{onset} (mV)	η_{10} (mV)	Tafel slope (mV dec^{-1})	Reference
N-Mo$_2$C/CFP-45	**23**	**80**	**65**	**This work**
Co‑NRCNTs	330	540	--	[S7]
FeP nanoparticles	--	102	--	[S8]
Mo$_5$N$_6$	--	~249	330	[S10]
Ni$_2$P@NPCNFs	148	185.3	230.3	[S11]
MoP$_2$ NSs	--	85	98	[S12]
MoP NS/CC	--	187	94	[S13]
Ni$_3$S$_2$/NF	--	170	--	[S21]
3D MoS$_2$/N-GAs	236	261	230	[S22]
Co$_9$S$_8$@C	150	290	280	[S23]
FePSe$_3$/NC	--	140.1	167	[S17]
(CNF)@CoS$_2$	130	360	63.7	[S18]
Cu$_{0.075}$Co$_{0.925}$P/CP	--	120	97.5	[S19]

Table S6. Comparison of HER performances for N-Mo$_2$C/CFP-45 with other non-noble metal-based electrocatalysts in 1 M KOH.

Catalyst	η_{onset} (mV)	η_{10} (mV)	Tafel slope /mV dec^{-1}	Reference
N-Mo$_2$C/CFP-45	**6**	**36**	**32**	**This work**
Co－NRCNTs	160	370	--	[S7]
N,S-CN	--	380	103	[S24]
Mn-hcp Ni/C	39	105	68	[S25]
Co-Ex-MoS$_2$	15	89	53	[S26]
SWCNTs/MoSe$_2$:Mo$_2$C	--	89	--	[S27]
Mo$_5$N$_6$	--	94	130	[S10]
Mo$_1$N$_1$C$_2$	13	132	90	[S28]
MoB/g-C$_3$N$_4$	80	133	46	[S29]
Ni$_2$P@NPCNFs	89	104.2	79.7	[S11]
MoP$_2$ NSs	--	67	70	[S12]
FePSe$_3$/NC	--	118.5	88	[S17]
(CNF)@CoS$_2$	130	207	113.3	[S18]
Cu$_{0.075}$Co$_{0.925}$P/CP	--	70	55.1	[S19]

References

(S1) X. Zhang, X. Yu, L. Zhang, F. Zhou, Y. Liang, R. Wang, Adv. Funct. Mater. 2018, **28**, 1706523.

(S2) H. Vrubel, X. Hu, Angew. Chem. Int. Ed. 2012, **51**, 12703-12706.

(S3) M. Xiang, D. Li, W. Li, B. Zhong, Y. Sun, Catal. Commun. 2007, **8**, 513-518.

(S4) Y. Huang, Q. Gong, X. Song, K. Feng, K. Nie, F. Zhao, Y. Wang, M. Zeng, J. Zhong, Y. Li, ACS Nano, 2016, **10**, 11337-11343.

(S5) S. Grimme, J. Antony, S. Ehrlich, H. Krieg, J. Chem. Phys. 2010, **132**, 154104-154113.

(S6) B. Delley, J. Chem. Phys. 2000, **113**, 7756-7764.

(S7) X. Zou, X. Huang, A. Goswami, R. Silva, B. R. Sathe, E. Mikmeková, T. Asefa, Angew. Chem. Int. Ed. 2014, **53**, 4372-4376.

(S8) J. F. Callejas, J. M. McEnaney, C. G. Read, J. C. Crompton, A. J. Biacchi, E. J. Popczun, T. R. Gordon, N. S. Lewis, R. E. Schaak, ACS Nano 2014, **8**, 11101-11107.

(S9) F. Li, X. Zhao, J. Mahmood, M. S. Okyay, S. M. Jung, I. Ahmad, S. J. Kim, G. F. Han, N. Park, J. B. Baek, ACS Nano 2017, **11**, 7527-7533.

(S10) H. Jin, X. Liu, A. Vasileff, Y. Jiao, Y. Zhao, Y. Zheng, S. Z. Qiao, ACS Nano 2018, **12**, 12761-12769.

(S11) M. Q. Wang, C. Ye, H. Liu, M. Xu, S. J. Bao, Angew. Chem. Int. Ed. 2018, **57**, 1963-1967.

(S12) W. Zhu, C. Tang, D. Liu, J. Wang, A. M. Asiri, X. Sun, J. Mater. Chem. A 2016, **4,** 7169-7173.

(S13) Z. Pu, S. Wei, Z. Chen, S. Mu, Appl. Catal., B 2016, **196**, 193-198.

(S14) L. Liao, S. Wang, J. Xiao, X. Bian, Y. Zhang, M. D. Scanlon, X. Hu, Y. Tang, B. Liu, H. H. Girault, Energy Environ. Sci. 2014, **7**, 387-392.

(S15) H. Lin, N. Liu, Z. Shi, Y. Guo, Y. Tang, Q. Gao, Adv. Funct. Mater. 2016, **26**, 5590-5598.

(S16) Y. Zhao, K. Kamiya, K. Hashimoto, S. Nakanishi, J. Am. Chem. Soc. 2015, **137**, 110-113.

(S17) J. Yu, W.-J. Li, H. Zhang, F. Zhou, R. Li, C.-Y. Xu, L. Zhou, H. Zhong, J. Wang, Nano Energy 2019, **57**, 222-229.

(S18) H. Gu, Y. Huang, L. Zuo, W. Fan, T. Liu, Inorg. Chem. Front. 2016, **3**, 1280-1288.

(S19) L. Yan, B. Zhang, J. Zhu, S. Zhao, Y. Li, B. Zhang, J. Jiang, X. Ji, H. Zhang, P. K. Shen, J. Mater. Chem. A 2019, **7**, 14271-14279.

(S20) G. Humagain, K. MacDougal, J. MacInnis, J. M. Lowe, R. H. Coridan, S. MacQuarrie, M. Dasog, Adv. Energy Mater. 2018, **8**, 1801461-1801466.

(S21) L. L. Feng, G. Yu, Y. Wu, G. D. Li, H. Li, Y. Sun, T. Asefa, W. Chen, X. Zou, J. Am. Chem. Soc. 2015, **137**, 14023-14026.

(S22) Y. Hou, B. Zhang, Z. Wen, S. Cui, X. Guo, Z. He, J. Chen, J. Mater. Chem. A 2014, **2,** 13795-13800.

(S23) L. L. Feng, G. D. Li, Y. Liu, Y. Wu, H. Chen, Y. Wang, Y. C. Zou, D. Wang, X. Zou, ACS Appl. Mater. Interfaces 2015, **7,** 980-988.

(S24) K. Qu, Y. Zheng, X. Zhang, K. Davey, S. Dai, S. Z. Qiao, ACS Nano 2017, **11,** 7293-7300.

(S25) Q. Shao, Y. Wang, S. Yang, K. Lu, Y. Zhang, C. Tang, J. Song, Y. Feng, L. Xiong, Y. Peng, Y. Li, H. L. Xin, X. Huang, ACS Nano 2018, **12,** 11625-11631.

(S26) Y. Luo, X. Li, X. Cai, X. Zou, F. Kang, H. M. Cheng, B. Liu, ACS Nano 2018, **12,** 4565-4573.

(S27) L. Najafi, S. Bellani, R. Oropesa-Nunez, M. Prato, B. Martin-Garcia, R. Brescia, F. Bonaccorso, ACS Nano 2019, **13,** 3162-3176.

(S28) W. Chen, J. Pei, C. T. He, J. Wan, H. Ren, Y. Zhu, Y. Wang, J. Dong, S. Tian, W. C. Cheong, S. Lu, L. Zheng, X. Zheng, W. Yan, Z. Zhuang, C. Chen, Q. Peng, D. Wang, Y. Li, Angew. Chem. Int. Ed. 2017, **56,** 16086-16090.

(S29) Z. Zhuang, Y. Li, Z. Li, F. Lv, Z. Lang, K. Zhao, L. Zhou, L. Moskaleva, S. Guo, L. Mai, Angew. Chem. Int. Ed. 2018, **57**, 496-500.